NANOTHERMOMETRY

Imaging of nonlocal hot-electron energy dissipation via shot noise

Qianchun Weng,[1,4]* Susumu Komiyama,[1,5]* Le Yang,[2] Zhenghua An,[2,3]† Pingping Chen,[1] Svend-Age Biehs,[6] Yusuke Kajihara,[4] Wei Lu[1]†

In modern microelectronic devices, hot electrons accelerate, scatter, and dissipate energy in nanoscale dimensions. Despite recent progress in nanothermometry, direct real-space mapping of hot-electron energy dissipation is challenging because existing techniques are restricted to probing the lattice rather than the electrons. We realize electronic nanothermometry by measuring local current fluctuations, or shot noise, associated with ultrafast hot-electron kinetic processes (~21 terahertz). Exploiting a scanning and contact-free tungsten tip as a local noise probe, we directly visualize hot-electron distributions before their thermal equilibration with the host gallium arsenide/aluminium gallium arsenide crystal lattice. With nanoconstriction devices, we reveal unexpected nonlocal energy dissipation at room temperature, which is reminiscent of ballistic transport of low-temperature quantum conductors.

In modern downscaled microelectronics, current-carrying charges are locally driven far from equilibrium, and the associated heat dissipation is seen as a major concern for future development (*1*). Optimizing nanoscale thermal management by understanding and controlling hot-carrier kinetics is needed to make progress in post–Moore-era nanoelectronics (*1*, *2*). Particularly, understanding the mechanism of heat exchange between the electron and lattice systems is desirable in order to approach ideal device functionality (*1*–*3*). Meanwhile, the excess energy of hot electrons along with a variety of their rich interactions provide a number of promising applications, such as hot luminescent light sources (*4*, *5*), broadband photodetectors (*6*), highly efficient solar cells (*7*), thermoelectric devices (*8*), and plasmon-enhanced photochemistry (*9*). However, it remains extremely challenging to directly map hot electrons in real space with nanoscale resolution (*10*). Pump-probe techniques (*11*, *12*) provide a powerful tool for probing ultrafast transient phenomena with highest resolutions, both in spatial and temporal domains, but cannot be applied to study electronic devices in operating steady state. Sensitive nanothermometry techniques have been developed recently such as scanning thermal microscope (*13*), microscopic Raman spectroscopy (*14*), and plasmon resonance microscopy (*15*). The effective temperature of nonequilibrium electrons, however, is difficult to access with these techniques because electronic nanothermometry is fundamentally hindered by the fact that the heat capacity of electrons is intrinsically small: It is typically several orders of magnitude less than that of the lattice (*16*). Hot electrons are hence easily disturbed by probe-induced local heat flow in most of the nanothermometry techniques.

As a sensitive probe of the electron system, we focus on current fluctuations induced by nonequilibrium electrons, or shot noise (*17*), which has proven to contain nanoscopic information of electron motion not obtained from standard resistance measurements (*17*–*20*). Despite decades of extensive studies, the real-space characteristics of shot noise have been unknown because the existing noise probes were physically immobile (*21*, *22*). In addition, experiments have not been able to access noise frequencies higher than a few hundred gigahertz (*20*), which is far below the typical intrinsic scattering rate of hot electrons; thus, important signatures of ultrafast phenomena have remained obscure.

Here, we visualize hot electrons via shot noise by using a scattering type scanning near-field optical microscope (s-SNOM) (*23*–*26*) called the scanning noise microscope (SNoiM) [Fig. 1A and section 1 of (*27*)]. Current fluctuations induced by nonequilibrium electrons generate fluctuating electromagnetic (EM) evanescent fields on the material surface. In our SNoiM, a sharp metal tip scatters the fluctuating EM evanescent fields to be collected by a confocal microscope and detected with an ultrahighly sensitive sensor called a charge-sensitive infrared phototransistor (*28*). The frequency bandwidth of detection is $\omega/2\pi$ = 21.3 ± 0.7 THz, which is well away from the surface phonon polariton resonance frequencies of the host crystal, so that the measurement is relatively insensitive to phonons. The spatial resolution of the image is ~50 nm. The fluctuating EM evanescent fields detected by SNoiM are, in general, excited not only by nonequilibrium current fluctuation (excess noise) (*17*) but also by thermal current fluctuation in thermal equilibrium conditions (Nyquist noise) (*22*, *29*): The excess noise is specifically termed shot noise if it is caused by nonequilibrium charge carriers. The excellent imaging capability and sensitivity of SNoiM have been proven in recent experiments on metals (*26*).

Below, we will call the signal coming from the tip-scattered EM evanescent fields the passive near-field (NF) signal. In the measurements, the small NF signal component has to be distinguished from a much stronger component associated with the unwanted far-field (FF) background radiation. To this end, two different methods were applied [section 1 of (*27*)]. In one method, the tip height is modulated at f = 5 Hz as a square wave alternating between h and $h + \Delta h$, where Δh = 100 nm throughout this work. The difference signal, $V_{sig}(h) - V_{sig}(h + \Delta h)$, is obtained by demodulating the detector output at fundamental frequency (5 Hz). This difference signal practically equals the signal $V_{sig}(h)$ at h because the NF signal intensity rapidly decreases with increasing h so that $V_{sig}(h + \Delta h)$ can be practically ignored for Δh = 100 nm. In the other method, the bias voltage applied to the device is modulated as a square wave alternating between 0 and V_b at 5 Hz, while the tip height h is not modulated, and the signal is obtained by demodulating the detector output at 5 Hz.

We study small conductors harboring a quasi–two-dimensional electron gas (2DEG), in which energy injection can be highly localized in real space, making hot-electron effects explicit, as theoretically predicted (*30*). The devices with narrow constriction (Fig. 1B and fig. S2) are fabricated in a GaAs/AlGaAs quantum well structure with a 2DEG layer buried 13 nm below the surface [sections 2 and 3 of (*27*)]. Figure 1C shows a two-dimensional (2D) image of the NF signal intensity obtained through the tip-height modulation method with h = 10 nm and bias voltage of V_b = +6 V. In and around the constriction, the region of high NF signal expands toward the downstream side of the electron flow (the positive voltage side). Figure 1D shows that the asymmetric feature is reversed in the opposite polarity of bias voltage (V_b = −6 V), suggesting that the effect is intrinsic, rather than being caused by sample inhomogeneity.

We have cross-checked the signal by applying the V_b-modulation method (0V and ±6 V) with the tip height fixed at h = 10 nm; the obtained 2D images (fig. S3) and those of Fig. 1, C and D, were in close agreement. For all the signals reported below, the two methods were found to yield signals that were nearly equal to each other in amplitude and qualitative features [see section 1 of (*27*) for a discussion]. This indicates that the signals are free from the unwanted FF radiation component and that the thermally generated components are negligible; therefore, the signal

[1]National Laboratory for Infrared Physics, Shanghai Institute of Technical Physics, The Chinese Academy of Sciences, Shanghai 200083, PR China. [2]State Key Laboratory of Surface Physics, Institute for Nanoelectronic Devices and Quantum Computing, and Key Laboratory of Micro and Nano Photonics Structures (Ministry of Education), Department of Physics, Fudan University, Shanghai 200433, PR China. [3]Collaborative Innovation Center of Advanced Microstructures, Nanjing 210093, PR China. [4]Institute of Industrial Science, The University of Tokyo, Komaba 4-6-1, Meguro-ku, Tokyo, 153-8505, Japan. [5]Department of Basic Science, The University of Tokyo, Komaba 3-8-1, Meguro-ku, Tokyo, 153-8902, Japan. [6]Institut für Physik, Carl von Ossietzky Universität, D-26111 Oldenburg, Germany.
*These authors contributed equally to this work.
†Corresponding author. Email: anzhenghua@fudan.edu.cn (Z.A.); luwei@mail.sitp.ac.cn (W.L.)

is caused by the current-induced current fluctuation or excess noise [section 1 of (*27*)]. The excess noise originates from either heated 2DEG or heated lattice. To distinguish between the two, we note that the experimentally obtained images of the NF signal are confined within the mesa structure where the 2DEG is present, with a sharp cut-off edge at the boundary [fig. S5B and section 4 of (*27*)]. This indicates that the origin of the signal is the 2DEG because lattice heating (or nonequilibrium phonon distribution) would not be confined to the mesa structure, and the border of the heated region would have to be substantially smoothed by diffusion of phonons over a relaxation length (200 to 300 nm) (*31*). Thus, the NF signal is ascribed to the shot noise caused by heated 2DEG; this conclusion is strongly supported by theoretical estimates [sections 5 and 6 of (*27*)].

The second important feature is the rapid decay of the NF signal with increasing h (Fig. 1E), where the NF signal is taken via V_b-modulation and is plotted against h. The decay curve is well reproduced with a theoretical predicted curve obtained by combining the hot-electron concept with the electromagnetic local density of states (EM-LDOS) (*32*) of the fluctuating EM evanescent fields [fig. S8 and sections 5 to 7 of (*27*)].

Figure 2, A to F, displays images of the NF signal obtained by modulating the tip height with h = 10 nm and shows how the hot-electron distribution evolves with increasing V_b. NF signals caused by hot electrons are discernible when V_b reaches ~0.8 V, and their distribution expands toward the downstream side of the constriction when V_b exceeds ~4.0 V. At higher values of V_b, a distinct hot spot develops outside the constriction (Fig. 2F for V_b ~ 8.0 V); the signal intensity increases as the electrons move away from the constriction, creating the hottest spot at a distance 200 to 300 nm away from the constriction. This feature is elucidated in Fig. 2G, which shows a distinct maximum peak of the NF signal intensity developing at a position ($y \approx +250$ nm) shifted from the constriction for 5 V < V_b. The nonlocal feature of power dissipation, along with the current-voltage characteristics similar to those described above, have been found in devices with different constriction patterns and crystallographic orientations, suggesting the intrinsic nature of the phenomena [fig. S4 and section 4 of (*27*)]. Above V_b ~ 4.0 V, the current saturates (Fig. 2H). Interestingly, the NF signal intensity at the constriction center ($y \approx 0$) is saturated in step with the current saturation, but the one at the off-centered hot spot ($y \approx +250$ nm) continues to increase. The NF signal intensity for $V_b < 3$ V is roughly proportional to the current I, which is consistent with the conventional theory of shot noise, $\langle S_{shot} \rangle \propto 2e|I|$ (where e is the unit charge). The lack of saturation of the signal intensity at the shifted hot spot for $V_b > 4$ V suggests that specific hot-electron processes play a role, as will be discussed later.

The discrepancy between the noise profile and the electric field distribution is confirmed in additional experiments, where electrostatic potential distribution around the constriction is studied by biasing the metal tip in scanning gate microscopy (SGM) [fig. S10 and section 8 of (*27*)]. A region of high electric fields is found to be concentrated symmetrically in a narrow region around the constriction, roughly defined by $|y| <$ 250 nm. The hot-electron distribution (Fig. 2, D to F), therefore, develops beyond the region of high electric fields. SGM measurements show that the electric field at the constriction reaches $E_c \approx 104$ kV/cm for $V_b = 9.0$ V. The E_c values have been derived as a function of V_b in an independent method, yielding results consistent with SGM (fig. S11).

For materials in thermal equilibrium (*23*–*26*), NF signals have been quantitatively understood in the theoretical framework based on the EM-LDOS for thermally excited fluctuating EM evanescent fields (Nyquist noise) [section 5 of (*27*)]. In nonequilibrium conditions, rigorous theory is not available in general. However, the "hot-electron concept" (*17*, *18*) is applicable in our system, and the knowledge established in thermal equilibrium can be employed as the first-order approximation by considering an effective electron temperature T_e [section 6 of (*27*)]. In our GaAs devices, the exchange of energy and momentum among electrons is so efficient as to nearly establish a quasi-equilibrium state within the electron system. It then follows that the resulting nonequilibrium distribution function of electrons is approximated by the equilibrium Fermi distribution function characterized by an effective electron temperature T_e, and many physical quantities can be derived approximately by noting only the effective temperature T_e. Particularly, the shot noise is approximated by the Nyquist noise at $T = T_e$ and is known by the term hot-electron shot noise (*17*, *18*). In this work, T_e is estimated from the NF signal intensity (see color scales in Figs. 1 and 2) and provides an approximate measure of the average kinetic energy of electrons $\langle \varepsilon \rangle \equiv (3/2)\, k_B T_e$ [section 7 of (*27*)]. The estimated values—T_e = 2200 to 2500 K or $\langle \varepsilon \rangle$ = 280 to 320 meV at the hot spot (Fig. 2F)—are consistent, within the accuracy of estimation (± 7%), with the noise temperature reported in microwave noise measurements on short channel n-GaAs devices (*20*) and with the values $\langle \varepsilon \rangle$ = 300 to 550 meV predicted in Monte Carlo simulations (*33*), both at an electric field $E \approx 100$ kV/cm [section 7 of (*27*)].

The nonlocal feature in this work is reminiscent of the phase-coherent transport through low-dimensional conductors (*34*) or ballistic transport through quantum point contacts at low temperatures (*35*), where energy is dissipated in reservoirs rather than in conductors themselves. The simplest interpretation is therefore to assume purely ballistic motion of electrons passing through the constricted region. Nonlocal energy dissipation is expected to occur in diffusive transport as well (*36*), because electrons necessarily travel a certain distance after acceleration until they release excess energy to the lattice by phonon emission. Indeed, it is a commonly expected feature in most of modern high-speed short-channel transistors (*37*).

We quantitatively model electron transport through the constriction by taking into account relevant transport parameters [section 3 of (*27*)]. When electrons approach and enter the constricted region from the negative-voltage side, they are accelerated by the electric fields. When the accelerated electrons pass through and exit from the constriction, they, in turn, cool down

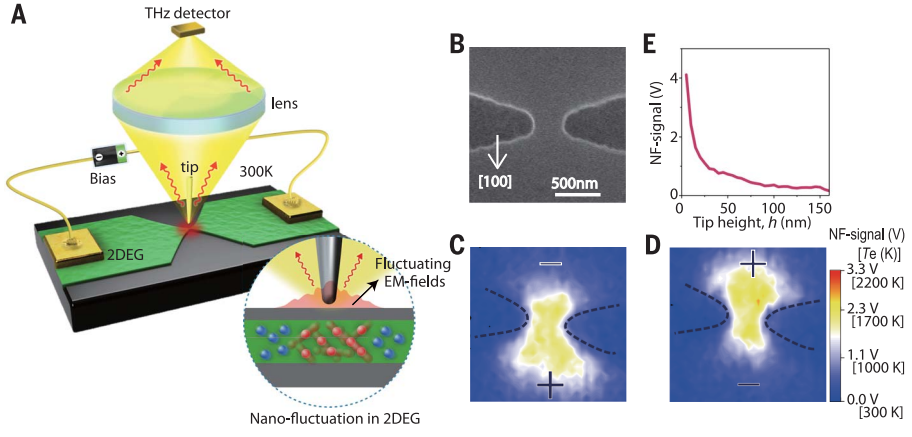

Fig. 1. Nanoscale mapping of ultrahigh-frequency excess noise (21.3 ± 0.7 THz) with scanning noise microscope (SNoiM). (**A**) Schematic representation of the experimental setup of SNoiM [section 1 of (*27*)]. (**B**) SEM image of the nanodevice with a constriction fabricated in a GaAs/AlGaAs quantum well (QW) structure. (**C** and **D**) Two-dimensional real-space images of the NF signal intensity (excess noise), for opposite bias polarities (±6 V). The horizontal and vertical scales are those of the SEM image of (B). The NF signals are taken by modulating the tip height. The color scale is given by the signal amplitude V (detector output) as well as by the effective electron temperature T_e (K) [section 7 of (*27*)]. The electric field at the constriction is estimated to be $E_c \approx 62$ kV/cm for $V_b = 6.0$ V. (**E**) Decay profile of the NF signal with increasing the tip-height h from 5 nm to 150 nm, taken at the center of constriction with $V_b = 6$ V. The signal is obtained by modulating V_b between 0 and 6 V without modulating the tip height.

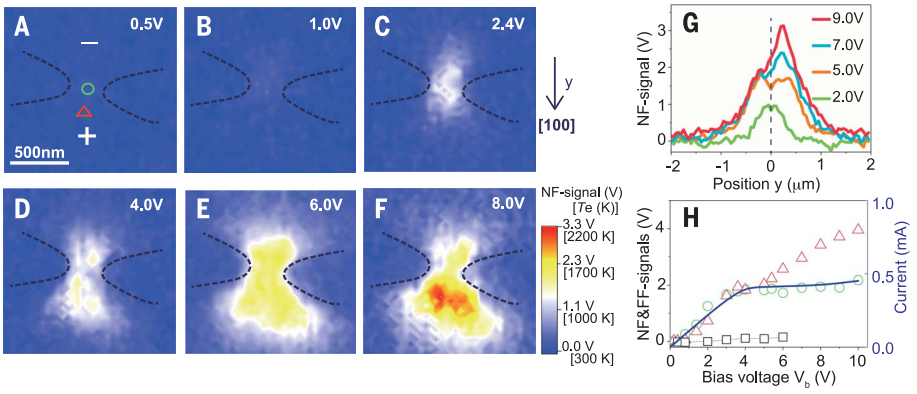

Fig. 2. Evolution of the excess noise distribution with increasing bias voltage, V_b. (**A** to **F**) Two-dimensional images obtained by modulating the tip height. The crystallographic orientation is *y*//[100]. (**G**) One-dimensional profile of the NF signal intensity in the *y* direction, where $y = 0$ corresponds to the center point of the constriction marked by the green circle in Fig. 2A. The data are taken by modulating V_b. (**H**) The solid line shows the current versus V_b curve. Green circles and red triangles show, respectively, the NF signals (excess noise intensities) at the positions marked by o ($y = 0$) and Δ ($y = +250$ nm) in Fig. 2A. The data are taken by modulating V_b. The black squares plot the FF signal, obtained by modulating V_b without using the tip, showing that the current-induced FF component is less than a few percent of the NF signal.

by releasing their excess energy to the lattice. The cooling-down process is, however, relatively slow because the energy relaxation time due to electron-phonon interaction is relatively long ($\tau_{e\text{-}ph} \approx 1.1$ ps). The energetic electrons, on the other hand, pass through the constricted region at high velocities, $v_d \approx (1.9 \text{ to } 2.1) \times 10^5$ m/s (velocity overshoot) (*20*, *38*). It follows that the energetic electrons drift a large distance, $L_{drift,e\text{-}ph} = v_d\tau_{e\text{-}ph} = 210$ to 230 nm, before being equilibrated with the lattice.

The feature of nonlocal energy dissipation is enhanced further by the transfer of hot electrons to upper satellite valleys (*20*, *33*) [section 9 of (*27*)]. It is well known that hot electrons transfer from the Γ-valley to the satellite X- and/or L-valleys at high electric fields (*20*). The effective mass of electrons in the upper valleys is much larger than in Γ-valley, so conductance is reduced, causing the saturation of current *I* for 4.0 V < V_b or 15 kV/cm < E_c (Fig. 2H and figs. S4 and S11). In our system, electron transfer to X-valleys lying above the Γ-valley by $\Delta\varepsilon_{\Gamma X} \approx 550$ meV is important (*20*). The upper valleys serve as a storage for energetic electrons and intensify the feature of nonlocal power dissipation as described below.

A representative experimental image of hot electrons is shown in Fig. 3A, and a detailed interpretation of the nonlocal transport is illustrated in Fig. 3, B to D. The average kinetic energy and the fractional ratio of population of electrons in the Γ-valley are denoted, respectively, by $<\varepsilon_\Gamma>$ and n_Γ. As the electrons approach the constriction from the source side (α, −250 nm < *y* < 0 in Fig. 3A), the rapidly increasing electric fields accelerate the electrons (α in Fig. 3B), and the electrons increasingly transfer to the X-valleys (α in Fig. 3C). The average energy, $<\varepsilon_\Gamma>$, thereby increases, whereas the fractional population, n_Γ, decreases (α, −250 nm < *y* < 0 in Fig. 3D). At the center of the constriction (β, $y \approx 0$ in Fig. 3, C and D), $<\varepsilon_\Gamma>$ reaches maximum, whereas n_Γ falls to a minimum, $n_{\Gamma,c} = 0.3$ to 0.23 for $V_b = 6.0$ to 9.0 V ($E_c = 60$ to 120 kV/cm) (fig. S11). Despite the small $n_{\Gamma,c}$ value, the current through the constriction is dominated by the Γ-valley electrons because their "overshoot" drift velocity $v_{d,\Gamma} \approx (1.9 \text{ to } 2.1) \times 10^5$ m/s is much higher than the drift velocity of X-valley electrons. On the downstream side of the constriction, the electric field *E* decreases rapidly with increasing *y* (γ in Fig. 3B). The average energy $<\varepsilon_\Gamma>$ accordingly decreases, but the decrease is slow because (i) the longitudinal-optical-phonon emission process is relatively slow ($\tau_{e\text{-}ph} \approx 1.1$ ps) and (ii) the electrons stored in the X-valleys are now transferred back to the Γ-valley, supplying energetic electrons in the Γ-valley (γ in Fig. 3C). Therefore, n_Γ rapidly recovers the low-field value ($n_\Gamma \approx 1$), but $<\varepsilon_\Gamma>$ decreases much more slowly with increasing *y* ($0 < y < 250$ nm in Fig. 3D).

The excess noise is generated primarily by the Γ-valley electrons because their average kinetic energy $<\varepsilon_\Gamma>$ is much higher than that of X-valley electrons $<\varepsilon_X>$ (*34*). The noise power density is an increasing function of both $<\varepsilon_\Gamma>$ and n_Γ, and we simply assume $P_n = n_\Gamma<\varepsilon_\Gamma>$ to give a plausible measure of the noise intensity. The profile of P_n (Fig. 3D) reproduces the corresponding experimental feature (Fig. 2G) fairly well, yielding a prominent maximum peak at a location displaced ($y \approx 250$ nm) from the constriction. The saturation of noise intensity at the center point of the constriction (Fig. 2H, $y = 0$) stems from the fact that the increase in $<\varepsilon_{\Gamma,c}>$ with increasing V_b (E_c) is compensated by the decrease in $n_{\Gamma,c}$. The lack of saturation at the shifted hot spot (Fig. 2H, $y = 250$ nm) is a consequence of the fact that $n_{\Gamma,c}$ at $y \approx 250$ nm does not decrease substantially so that the effect of $<\varepsilon_{\Gamma,c}>$ increase is uncompensated.

SNoiM is applicable to any microelectronics devices of semiconductors, semimetals, and metals. In addition, it can be applied to explore a variety of exotic modes of charge-carrier dynamics in emerging material systems such as graphene (*39*), topological conductors, Weyl semimetals, and anomalous Hall-effect conductors. The target of SNoiM is not restricted to electron systems: For example, by detecting the noise in the frequency band of the surface phonon polariton resonance of the host crystal, the lattice dynamics will be exclusively probed. The sensitivity of our system, limited by the fluctuation of

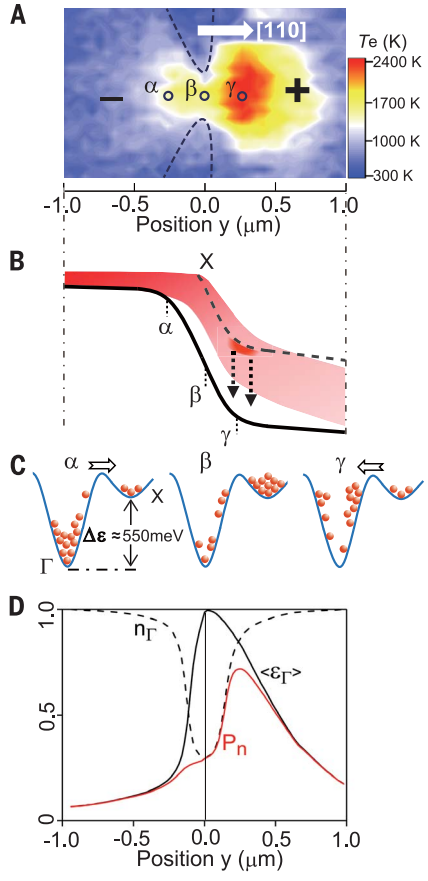

Fig. 3. Hot-electron kinetics in the vicinity of constriction. (**A**) Experimentally obtained image of the hot-electron distribution for $V_b = 9.0$ V ($E_c \approx 120$ kV/cm), taken in a different device from the one shown in Figs. 1 and 2. The data are taken by modulating the tip height with $h = 10$ nm. (**B**) Schematic representation of the electrostatic potential energy of the bottom of the conduction band: The solid line shows the Γ-valley and the broken line the X-valley. Shading shows the distribution of electrons. (**C**) Relative population of electrons in the Γ- and the X-valleys, respectively, at positions α, β, and γ in (A) and (B). (**D**) A sketch of the variation of n_Γ, $<\varepsilon_\Gamma>$, and $P_n = n_\Gamma<\varepsilon_\Gamma>$ along the *y* axis for $V_b = 6.0$ to 9.0 V, where $n_\Gamma \equiv N_\Gamma/N$ (N_Γ, the density of Γ-valley electrons; N, the total density of electrons) is the relative population of Γ-valley electrons, $<\varepsilon_\Gamma>$ is the average kinetic energy of Γ-valley electrons, and $P_n = n_\Gamma<\varepsilon_\Gamma>$ is a measure of the excess noise intensity.

background FF radiation, will be dramatically improved at cryogenic temperatures, making measurements in photon-counting mode possible (*40*). The fact that SNoiM should be operable over a range of temperatures with a tunable detection wavelength provides an advantage over most of existing nanothermometry techniques (*41*).

REFERENCES AND NOTES

1. M. M. Waldrop, *Nature* **530**, 144–147 (2016).
2. Y. Dubi, M. Di Ventra, *Rev. Mod. Phys.* **83**, 131–155 (2011).
3. J. Lee *et al.*, *Nat. Nanotechnol.* **9**, 101–105 (2014).
4. C. H. Cho, C. O. Aspetti, J. Park, R. Agarwal, *Nat. Photonics* **7**, 285–289 (2013).
5. M. Troccoli *et al.*, *Nature* **433**, 845–848 (2005).
6. N. M. Gabor *et al.*, *Science* **334**, 648–652 (2011).
7. D. J. Farrell, H. Sodabanlu, Y. Wang, M. Sugiyama, Y. Okada, *Nat. Commun.* **6**, 8685 (2015).
8. X. Cai *et al.*, *Nat. Nanotechnol.* **9**, 814–819 (2014).
9. Y. Zhai *et al.*, *Nat. Mater.* **15**, 889–895 (2016).
10. R. Chau, B. Doyle, S. Datta, J. Kavalieros, K. Zhang, *Nat. Mater.* **6**, 810–812 (2007).
11. E. Najafi, V. Ivanov, A. Zewail, M. Bernardi, *Nat. Commun.* **8**, 15177 (2017).
12. V. Jelic *et al.*, *Nat. Phys.* **13**, 591–598 (2017).
13. F. Menges *et al.*, *Nat. Commun.* **7**, 10874 (2016).
14. J. S. Reparaz *et al.*, *Rev. Sci. Instrum.* **85**, 034901 (2014).
15. M. Mecklenburg *et al.*, *Science* **347**, 629–632 (2015).
16. J. Y. Park, L. R. Baker, G. A. Somorjai, *Chem. Rev.* **115**, 2781–2817 (2015).
17. Y. M. Blanter, M. Büttiker, *Phys. Rep.* **336**, 1–166 (2000).
18. A. H. Steinbach, J. M. Martinis, M. H. Devoret, *Phys. Rev. Lett.* **76**, 3806–3809 (1996).
19. V. Bareikis, J. Liberis, I. Matulioniene, A. Matulionis, P. Sakalas, *IEEE Trans. Electron Dev.* **41**, 2050–2060 (1994).
20. V. Aninkevičius *et al.*, *Phys. Rev. B* **53**, 6893–6895 (1996).
21. E. S. Tikhonov *et al.*, *Sci. Rep.* **6**, 30621 (2016).
22. S. Kolkowitz *et al.*, *Science* **347**, 1129–1132 (2015).
23. Y. Kajihara, K. Kosaka, S. Komiyama, *Opt. Express* **19**, 7695–7704 (2011).
24. K. T. Lin, S. Komiyama, Y. Kajihara, *Opt. Lett.* **41**, 484–487 (2016).
25. K.-T. Lin, S. Komiyama, S. Kim, K. I. Kawamura, Y. Kajihara, *Rev. Sci. Instrum.* **88**, 013706 (2017).
26. S. Komiyama, Y. Kajihara, K. Kosaka, T. Ueda, Z. An, [cond-mat.mes-hall] (4 Jan 2016); available at https://arxiv.org/abs/1601.00368.
27. Materials and methods are available as supplementary materials.
28. S. Komiyama, *IEEE J. Sel. Top. Quantum Electron.* **17**, 54–66 (2011).
29. H. Nyquist, *Phys. Rev.* **32**, 110–113 (1928).
30. R. D'Agosta, N. Sai, M. Di Ventra, *Nano Lett.* **6**, 2935–2938 (2006).
31. L. Zeng *et al.*, *Sci. Rep.* **5**, 17131 (2015).
32. K. Joulain, R. Carminati, J.-P. Mulet, J.-J. Greffet, *Phys. Rev. B* **68**, 245405 (2003).
33. J. Požela, A. Reklaitis, *Solid-State Electron.* **23**, 927–933 (1980).
34. M. Büttiker, *Phys. Rev. Lett.* **57**, 1761–1764 (1986).
35. E. Tekman, S. Ciraci, *Phys. Rev. B* **42**, 9098–9103 (1990).
36. H. Pothier, S. Guéron, N. O. Birge, D. Esteve, M. H. Devoret, *Phys. Rev. Lett.* **79**, 3490–3493 (1997).
37. J. Schleeh *et al.*, *Nat. Mater.* **14**, 187–192 (2015).
38. S. L. Teitel, J. W. Wilkins, *IEEE Trans. Electron Dev.* **ED-30**, 150–153 (1983).
39. K. T. Lin *et al.*, IEEE *Xplore*; available at http://ieeexplore.ieee.org/document/8067243/).
40. K. Ikushima, in *Frontiers in Optical Methods, Springer Series in Optical Sciences*, K. Shudo, I. Katayam, Eds. (Springer Series in Optical Sciences, 2013), vol. 180, chap. 11.
41. D. Halbertal *et al.*, *Nature* **539**, 407–410 (2016).

ACKNOWLEDGMENTS

Z.A. thanks C. M. Hu, L. Zhou, S. W. Wu, and Y. F. Mei for helpful discussions. Part of the experimental work was carried out in Fudan Nanofabrication Laboratory. **Funding:** We acknowledge the research support from the National Natural Science Foundation of China under grant nos. 11427807/11634012/11674070, National Key Research Program of China under grant no. 2016YFA0302000, and Shanghai Science and Technology Committee under grant no. 16JC1400400. S.K. acknowledges support by the Chinese Academy of Sciences Visiting Professorships for Senior International Scientists. Q.W. is an International Research Fellow of the Japan Society for the Promotion of Science (JSPS). Y.K. acknowledges support from Collaborative Research Based on Industrial Demand by Japan Science and Technology Agency. **Author contributions:** S.K., Q.W., and Z.A. conceived the idea, analyzed the data, and cowrote the manuscript, with constant discussion with W.L. The SNoiM was constructed by Q.W. and Z.A. following the advice and the design of Y.K. and S.K. The experiments were carried out by Q.W. on nanodevices fabricated by L.Y. in the wafers grown by P.C. The simulation calculation of EM-LDOS was done by S.-A.B. The research projects were cosupervised by Z.A. and W.L. **Competing interests:** The authors declare no competing financial interests. **Data and materials availability:** All data needed to evaluate the conclusions in the paper are present in the paper and/or the supplementary materials. Spreadsheet data can be found at http://doi.org/10.5281/zenodo.1186949.

SUPPLEMENTARY MATERIALS

www.sciencemag.org/content/360/6390/775/suppl/DC1
Materials and Methods
Supplementary Text
Figs. S1 to S11
References (*42*–*57*)

16 February 2017; resubmitted 19 October 2017
Accepted 12 March 2018
Published online 29 March 2018
10.1126/science.aam9991

Imaging of nonlocal hot-electron energy dissipation via shot noise

Qianchun Weng, Susumu Komiyama, Le Yang, Zhenghua An, Pingping Chen, Svend-Age Biehs, Yusuke Kajihara and Wei Lu

Science **360** (6390), 775-778.
DOI: 10.1126/science.aam9991originally published online March 29, 2018

Taking the temperature of hot electrons

As electronic chips become smaller, efficient heat dissipation becomes a greater challenge. Electrons in such devices quickly accelerate over small distances, becoming "hot"—that is, out of equilibrium with the rest of the system. Weng *et al.* designed a thermometry probe that measures the effective temperature of hot electrons with a spatial resolution of about 50 nanometers. The method is based on the optical measurement of current noise and provides a glimpse into where heat is naturally dissipated in a working device.

Science, this issue p. 775